AIMS Materials Science, 6(3): 377–396.
DOI: 10.3934/matersci.2019.3.377
Received: 11 March 2019
Accepted: 09 May 2019
Published: 20 May 2019

http://www.aimspress.com/journal/Materials

Research article

Molecular dynamics simulation on mechanical behaviors of Ni_xAl_{100-x} nanowires under uniaxial compressive stress

Fu-Chieh Hsu and Tei-Chen Chen*

Department of Mechanical Engineering, National Cheng Kung Univversity, Tainan, Taiwan

*** Correspondence:** Email: ctcx831@mail.ncku.edu.tw; Tel: +88662757575; Fax: +88662352973.

Abstract: This article investigates the nanoscale mechanical properties and deformation mechanism of Ni_x–Al_{100-x} metallic glasses nanowires (NWs) subjected to uniaxial compressive stress. Molecular dynamics (MD) simulation is carried out using the program package LAMMPS with Embedded-Atom potential. Simulation is performed and focused on the effects of different slenderness ratio, quenching rate, alloy ratio, compression rate, temperature, defects and fracture process of Ni_x–Al_{100-x} metallic glasses NWs on the mechanical behaviors of these materials. Simulation results show that three possible deformation mechanisms, namely compressive deformation, buckling of structural instability, and lateral extrudes, may occur under different conditions. When the quenching rate is slow, the formation of amorphous phase after quenching is low, but both the corresponding ultimate stress and the Young's modulus become high. Moreover, under the same quenching rate, the ultimate stress increases with the decrease of the slenderness ratio. For different alloy ratio, it is found that B2 phase of this alloy system exhibits the highest magnitude of both ultimate stress and Young's modulus. In addition, the concentration effects of point defects on mechanical behaviors of materials are also evaluated and discussed.

Keywords: NiAl alloys; nanowires (NWs); molecular dynamics; slenderness ratio; buckling

1. Introduction

NiAl alloys have a great potential on the applications of the high temperature structures due to higher melting point, higher thermal conductivity, and lower density than Ni-based superalloys [1–6]. These alloys also offer excellent oxidation resistance at elevated temperatures. In recent decades, Lee et al. [7] have reported about the shear band formation and failure mechanism in monolithic glasses

and glass matrix composite by interrupted compression experiments. Alavi et al. [8] have examined the tensile failure of Ni–Al bimetallic nanowires under different strain rates and temperatures. When the NiAl alloys are cooled down from the melting point with sufficient high quenching rate, all the microstructures of the alloy become amorphous. They are then called NiAl metallic glasses (MGs). These kinds of materials have emerged as a prospective structural material in recent years. They possess excellent properties, such as high strength, high elastic limit, high ductility and superior corrosion resistance. Even though metallic glass has many beneficial applications, instantaneous brittle failure, however, leads to a fatal shortcoming. This phenomenon, however, may be different at the nanoscale [9–20]. Thus, it is important to understand the material deformation under applied strain at the nanoscale. Several papers have studied the mechanical properties of different alloys at the nanoscale. For instance, Wang et al. [21] have investigated the effects of nanoscale pores on the strength and ductility of porous $Cu_{46}Zr_{54}$ metallic glasses during nanoindentation and uniaxial compression tests using MD simulations. Wang et al. [22] have conducted uniaxial compression tests of slender metallic glass bars of composition $Zr_{52.5}Cu_{17.9}Ni_{14.6}Al_{10}Ti_5$ (at%). They found that the Zr-based metallic glass bars have a tendency to buckle elastically or plastically rather than to yield or fracture if its slenderness ratio is over a critical value. Wachter et al. [23] have reported the phenomenon of buckling in $Cu_{45}Zr_{45}Al_{10}$ metallic glass nanowires with different slenderness ratios by means of MD simulation. Sung and Chen [24] have investigated the crack growth and propagation of pre-cracked NiAl alloy prepared at different quenching rates under mode I loading conditions using MD. Zhuo and Beom [25] have investigated the mechanical properties of <100>-oriented square cross-sectional silicon nanowires under tension and compression, with a focus on the effect of side surface orientation. Moreover, the phenomena of stress-induced martensitic phase transformation in NiAl alloys have been investigated by MD [26,27]. They found that this transformation is reversible and is characterized by a significant temperature hysteresis. Recently, Mortazavi et al. [28] have examined the mechanical properties and thermal conductivity of graphitic carbon nitride by MD simulations. Properties of two main structures of triazine-based, g-C_3N_4 films were evaluated. This work investigates the mechanical properties and deformation mechanism of Ni_xAl_{100-x} alloy at the nanoscale under compressive stress. Effects of alloy ratio, quenching rate, slenderness ratio, temperature, strain rate, and point defect concentration on mechanical properties and deformation mechanism are evaluated and discussed.

2. Methodology

The MD simulations are carried out using the LAMMPS Package (Large-scale Atomic/Molecular Massively Parallel Simulator, http://lammps.sandia.gov). Several different crystalline phases of NiAl alloy can be found in the phase equilibrium diagram of NiAl binary alloy [29]. Specially, phase B2 (CsCl-type) plays the most important role in the NiAl alloy, which alloy ratio of Ni to Al is about 1 to 1 with the highest melting point. The ordered cubic B2 crystal structure of NiAl consists of two interpenetrating primitive cubic cells, where Al atoms occupy the cubic corners of one sublattice and Ni atoms occupy the cubic corners of the second sublattice. The ordering energy is believed very high which makes dislocation mobility rather difficult. Not only the physical model of $Ni_{50}Al_{50}$, four different alloy ratios ($Ni_{20}Al_{80}$, $Ni_{40}Al_{60}$, $Ni_{60}Al_{40}$ and $Ni_{80}Al_{20}$), as shown in Figure 1, are also investigated. The size of the initial model is 5 nm in diameter with round cross-section and 25~75 nm in length corresponding to the slenderness ratio (L/D) 5~15, where L

and D denote the length and diameter of NWs, respectively. The total number of atoms in each model with slenderness ratio ranged from 5 to 15 is about from 40000 to 120000. The atoms of Ni and Al are individually colored by blue and red. The atom velocities are adjusted in order to maintain them in an isothermal state with a specific temperature, and obeying Newton's second law. The model is initially relaxed at 300 K for 200 ps within a NPT (constant pressure and constant temperature) ensemble. The model is then heated up to 2300 K and kept for 50 ps, allowing the solid to melt using the conjugated gradient method. After that, the model is quenched to 100 K with a variable quenching rate ranging from 0.5 to 50 K/ps. The equilibrium microstructures of $Ni_{50}Al_{50}$ NWs at quenching rates of 0.5 and 50 K/ps are shown as in Figure 2a,b, respectively. At slow cooling rates, large grain sizes are formed, as shown in Figure 2a. On the other hand, at fast cooling rates, fine grain sizes are formed. If the cooling rate is high enough, as shown in Figure 2b, the atoms do not have enough time to rearrange themselves for further crystallization. The liquid state, consequently, maintains right up to the room temperature and then solidifies as metallic glass. During the deformation process, the model is compressed in the uniaxial direction. The many-body potential embedded atom method (EAM) [30] is employed in this work to describe the Ni–Ni, Al–Al and Al–Ni interactions. This intermolecular potential was proposed based on density functional theory and was capable of accurately calculating ground-state properties of realistic metal systems, such as the lattice constant, elastic constants, sublimation energy, and vacancy-formation energy.

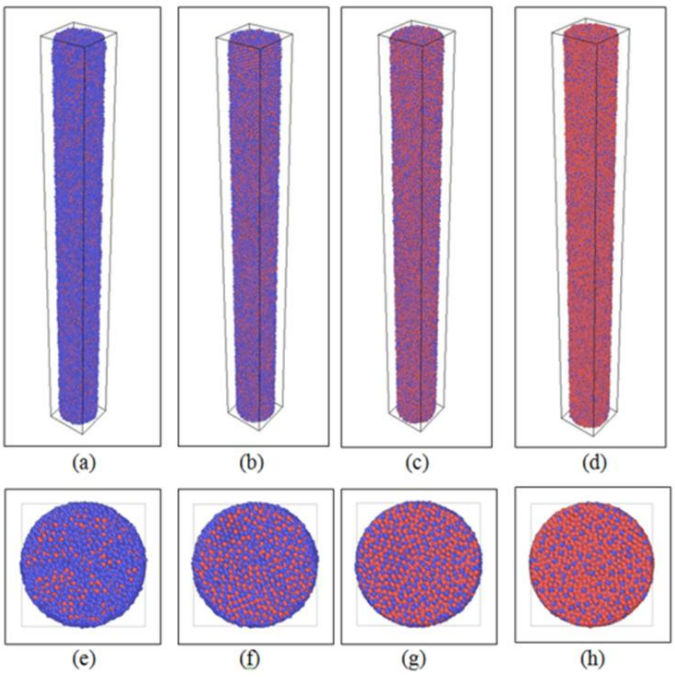

Figure 1. Physical models and cross-section of Ni_xAl_{100-x} NWs (a,e) $Ni_{20}Al_{80}$, (b,f) $Ni_{40}Al_{60}$, (c,g) $Ni_{60}Al_{40}$, (d,h) $Ni_{80}Al_{20}$ (purple: Al; red: Ni).

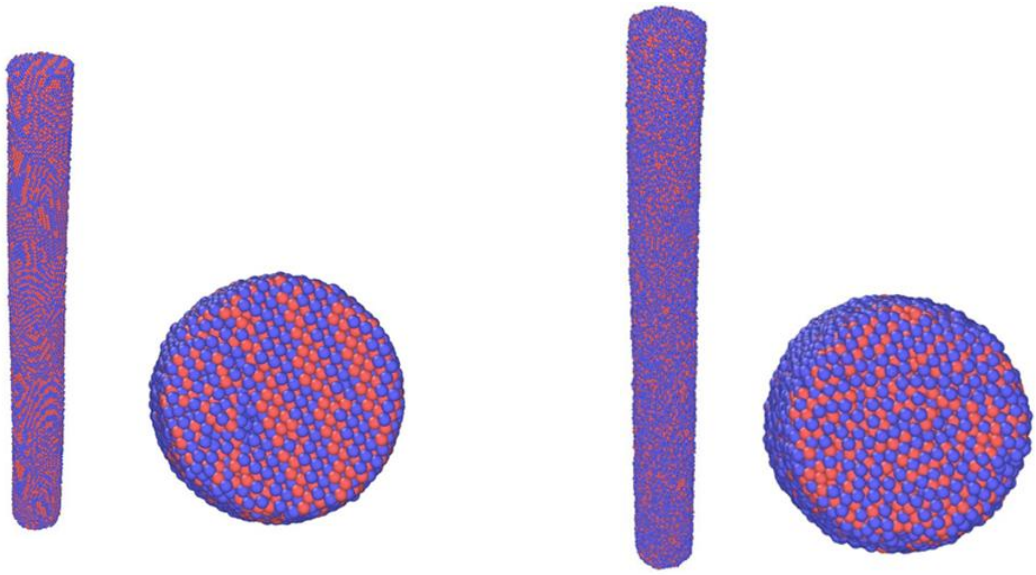

(a) (b)

Figure 2. Equilibrium microstructure of $Ni_{50}Al_{50}$ NWs at quenching rates of (a) 0.5 K/ps and (b)50 K/ps, respectively.

The time integration of motion is performed using Gear's fifth-order predictor-corrector method with a time step of 2 fs. To increase calculation efficiency, the Verlet neighbor-list method is used. The lists of neighbor atoms are calculated every 10 time steps with a cut-off radius of 0.65 nm. The interatomic stress of six components can be determined using virial stress and the von Mises effective stress to describe the mechanical properties.

$$\sigma_{mn} = \frac{1}{N}\sum_i \left[\frac{m v_i^m v_i^n}{V_i} - \sum_j \frac{\partial \phi(R_{ij})}{\partial R_{ij}} \frac{x_{ij}^m x_{ij}^n}{R_{ij}} \right] \tag{1}$$

$$V_i = \frac{4\pi}{3} a_i^3 \tag{2}$$

$$a_i = \frac{\sum r_{ij}^{-1}}{2\sum r_{ij}^{-2}} a_i^3 \tag{3}$$

$$\sigma' = \frac{1}{\sqrt{2}} \left[(\sigma_x - \sigma_y)^2 + (\sigma_y - \sigma_z)^2 + (\sigma_z - \sigma_x)^2 + 6(\tau_{xy}^2 + \tau_{yz}^2 + \tau_{zx}^2) \right]^{\frac{1}{2}} \tag{4}$$

In order to analyze the partial dislocations and stacking faults (SFs) during the compressive deformation, the technique of CSP [31] was used.

3. Results and discussion

The critical fundamental buckling stresses of $Ni_{50}Al_{50}$ NWs at different quenching rates are as

shown in Figure 3. It can be found that the simulated critical stresses are well consistent to the data proposed by modified Euler's formula [32] as the slenderness ratio is higher than 10. In other words, as slenderness is higher than 10, the NWs are mainly deformed by buckling rather than by elastic and/or plastic deformation. The formula is defined as follows

$$P_{\mathrm{cr}} = \eta \frac{\pi^2 (\mathrm{EI})^*}{L^2} + H, \quad H = 2\tau_0 D \tag{5}$$

where L is the effective length; η is a dimensionless constant; (EI)* denotes the effective bending rigidity; H is related to the surface residual tension τ_0.

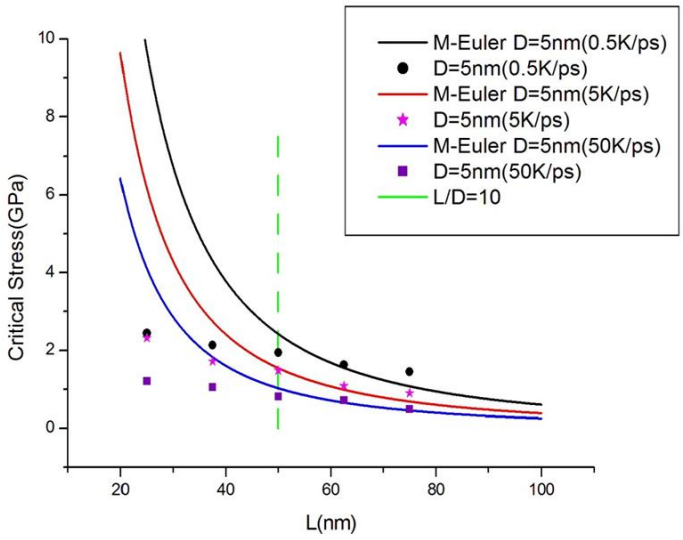

Figure 3. Critical stress of $Ni_{50}Al_{50}$ NWs at different quenching rates and slenderness ratios in comparison to modified Euler's formula.

Figure 4a,b shows the stress vs. strain curves of $Ni_{50}Al_{50}$ NWs with different slenderness ratio at quenching rates of 0.5 and 50 K/ps, respectively. It can be found that the ultimate stress is higher at slower quenching rate and smaller slenderness ratio due to a smaller amount of amorphous phase. Moreover, the NWs are deformed under compression without inducing structural buckling. On the other hand, a larger amount of amorphous phase is formed at faster quenching rate. The ultimate stress of this NW is lower than its crystalline counterpart. Moreover, remarkably sharper and narrower stress–strain curves appear. This phenomenon may be corresponded to the sudden drop in the compression resistance of materials due to either the initiation of buckling or the slipping induced extrudes along grain boundaries. It can be found that the structures with high slenderness ratio and coarse grains, generally fabricated under slow quenching rates, tend to exhibit sharp stress–strain curves. More detailed imagines of slipping induced extruding along grain boundaries can be observed in Figure 5. This figure illustrates the stress–strain curves, deformation mechanism, and distributions of local stress and strain of $Ni_{50}Al_{50}$ NWs with slenderness ratio of 10 and quenching rate of 0.5 K/ps. Since coarse-grained microstructures are generated under this slow quenching rate, slipping induced extrudes are easily occurred along the grain boundaries which are inclined approximately 45 degrees to the axial direction where the shear stress is maximum. The atomic

displacement vectors of the materials are as shown in Figure 6. It can be seen that the atoms near the grain boundaries tend to move along the grain boundaries and, finally, lead to the formation of extrudes as the strain is increasing. Moreover, as shown in Figure 7, the phenomena of extrudes are much easier induced rather than buckling. This phenomenon still occurs even when the slenderness ratio is as high as 15. In other words, phenomena of extrudes are the main deformation mechanisms and much more susceptible than buckling and compressible deformation for the materials with coarse grains when the slenderness ratio is smaller than 15.

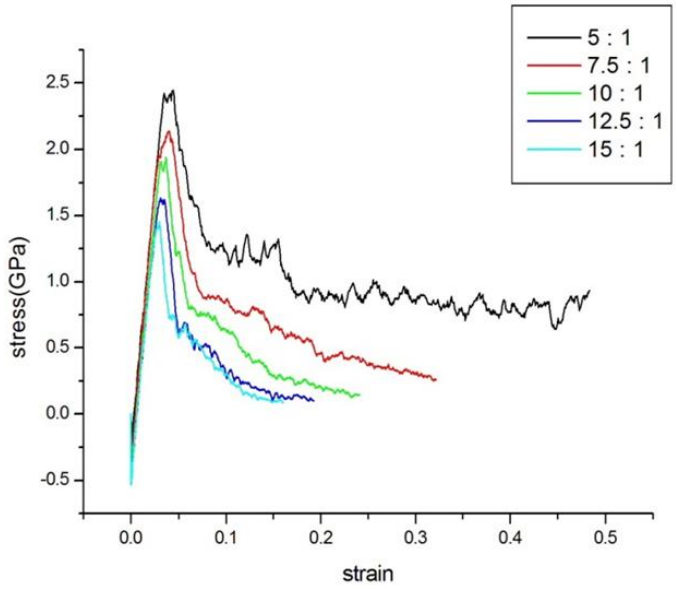

(a)

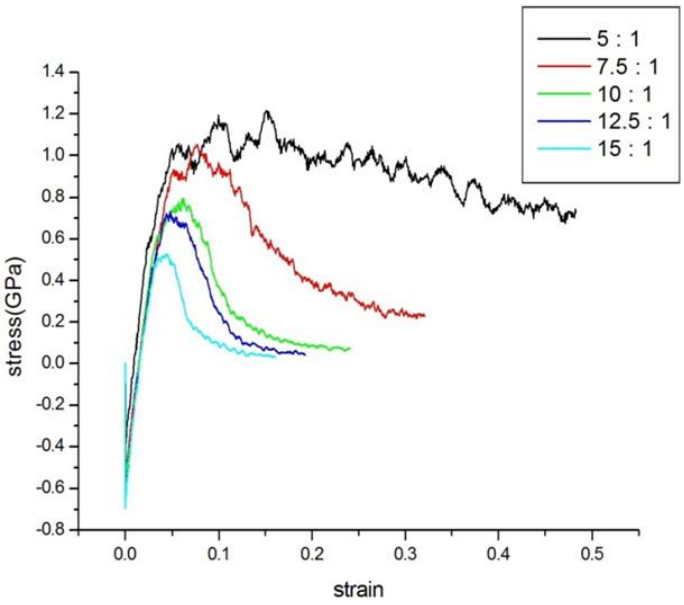

(b)

Figure 4. Stress–strain curves of $Ni_{50}Al_{50}$ NWs at quenching rates of (a) 0.5 K/ps and (b) 50 K/ps with different slenderness ratios (T = 100 K).

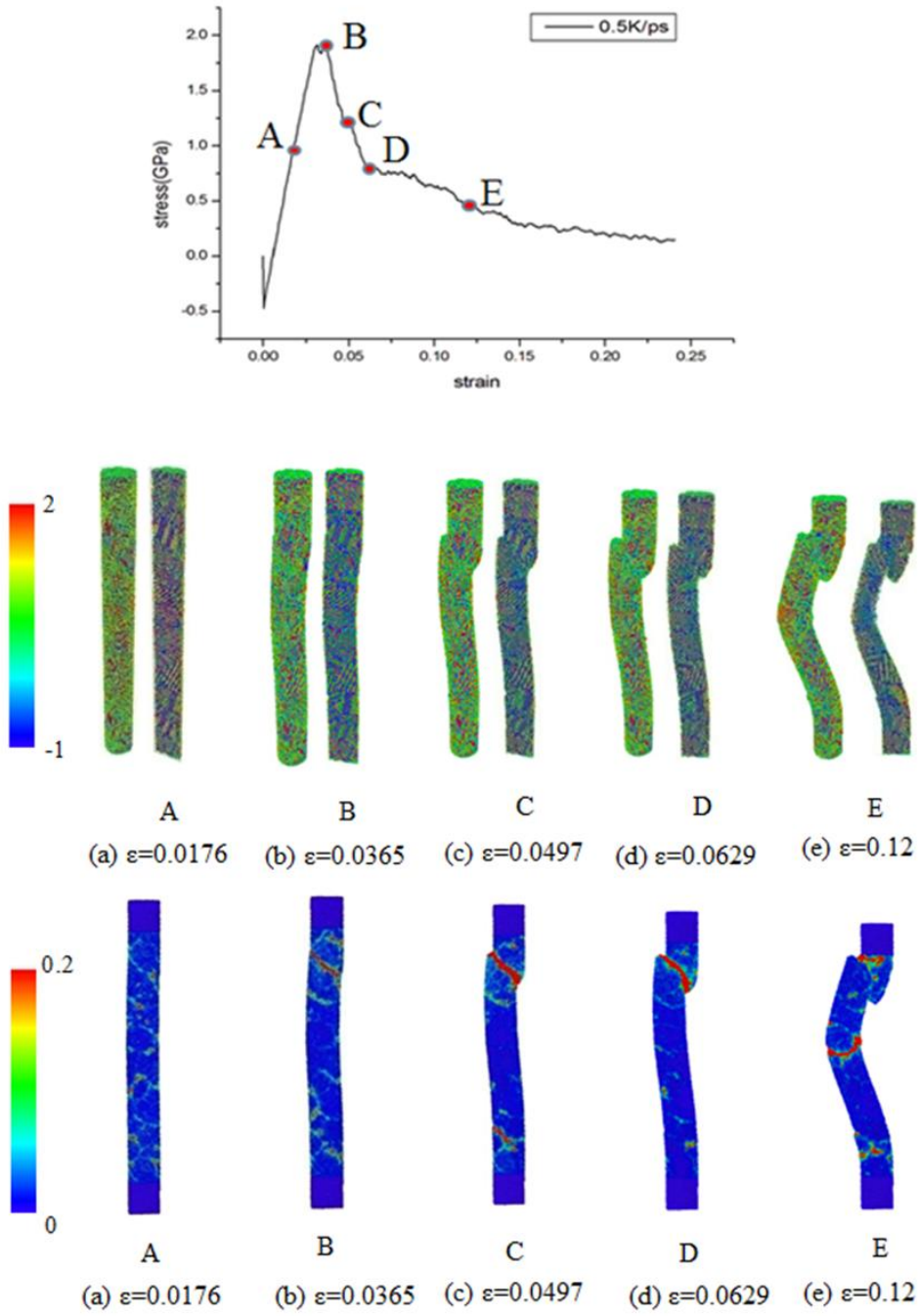

Figure 5. Stress–strain curves, deformation mechanism, and distributions of local stress (second row) and shear strain (third row) of $Ni_{50}Al_{50}$ NWs with quenching rates of 0.5 K/ps at different strains (L/D = 10).

On the other hand, the deformation mechanism of $Ni_{50}Al_{50}$ NWs at quenching rate of 50 K/ps with slenderness ratio of 10 is as shown in Figure 8. Since amorphous phase becomes dominant under this fast quenching rate, all the atoms of materials tend to move uniformly along the compressive axial direction as the strain gradually increases, as shown in Figure 9. The stress–strain curves then start to drop as the phenomenon of buckling starts to take place. Figure 10 illustrates the deformation mechanism of NWs when the slenderness ratio is ranged between 5 and 15. It is found

that since amorphous phase becomes dominant under this situation, the NWs cannot produce deformation along the slip system of the crystalline phases. Consequently, both the compressive deformation with shear band and the phenomenon of buckling take place together. The former, however, is dominant at the low slenderness ratio, while the latter is dominant at the large slenderness ratio. In addition, it appears that the amorphous phase in NWs is stable and remains unchanged as the strain increases.

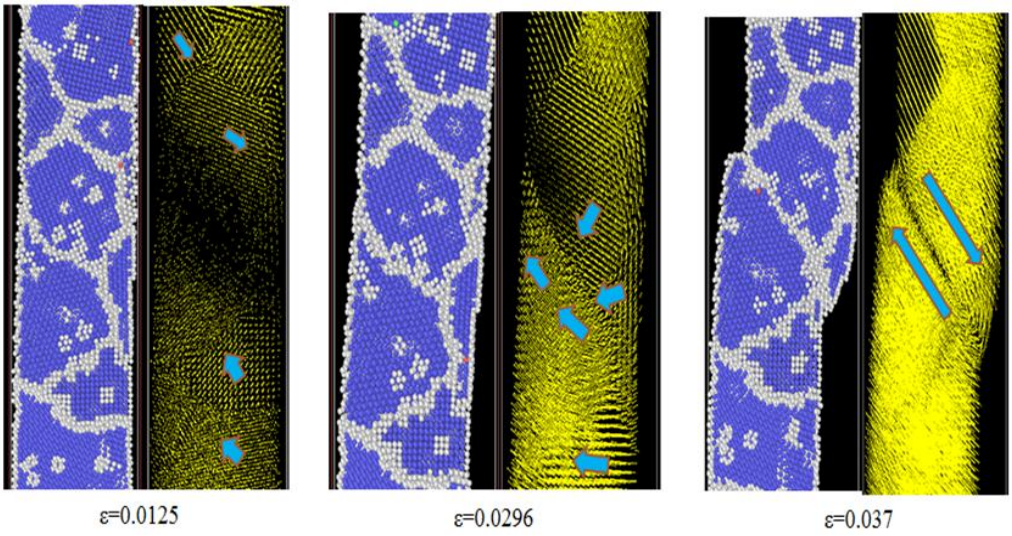

Figure 6. Atomic displacement vectors (RHS of each strain level) and distributions of microstructures (LHS: gray: amorphous; blue: BCC) of $Ni_{50}Al_{50}$ NWs at different strains with quenching rates of 0.5 K/ps (L/D = 15, T = 100 K).

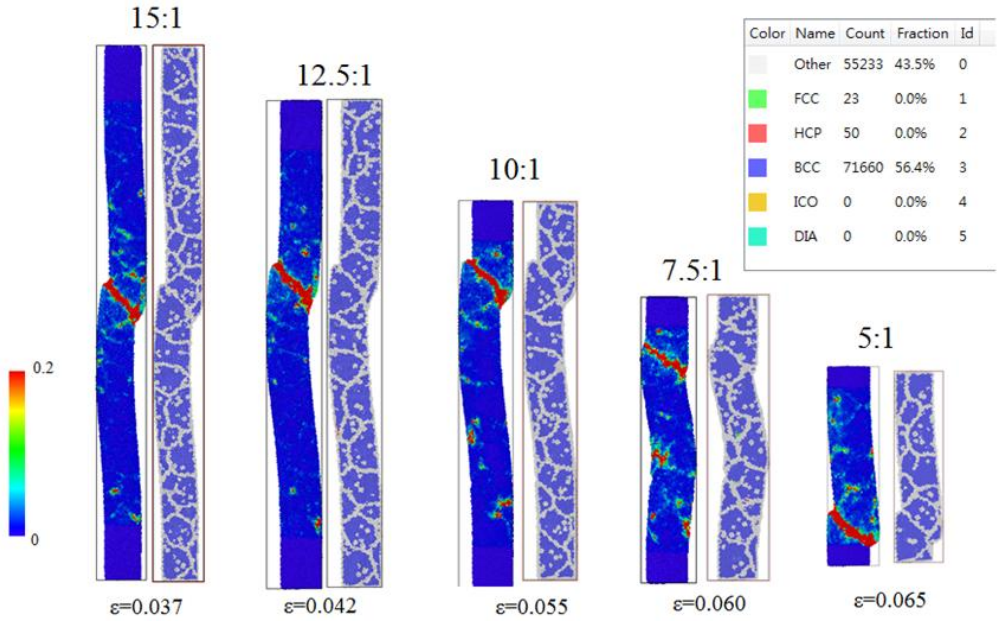

Figure 7. Deformation pattern as well as distributions of local shear strain (LHS of each strain level) and microstructures (RHS: gray: amorphous; blue: BCC) of $Ni_{50}Al_{50}$ NWs at different slenderness ratios with quenching rates of 0.5 K/ps (T = 100 K).

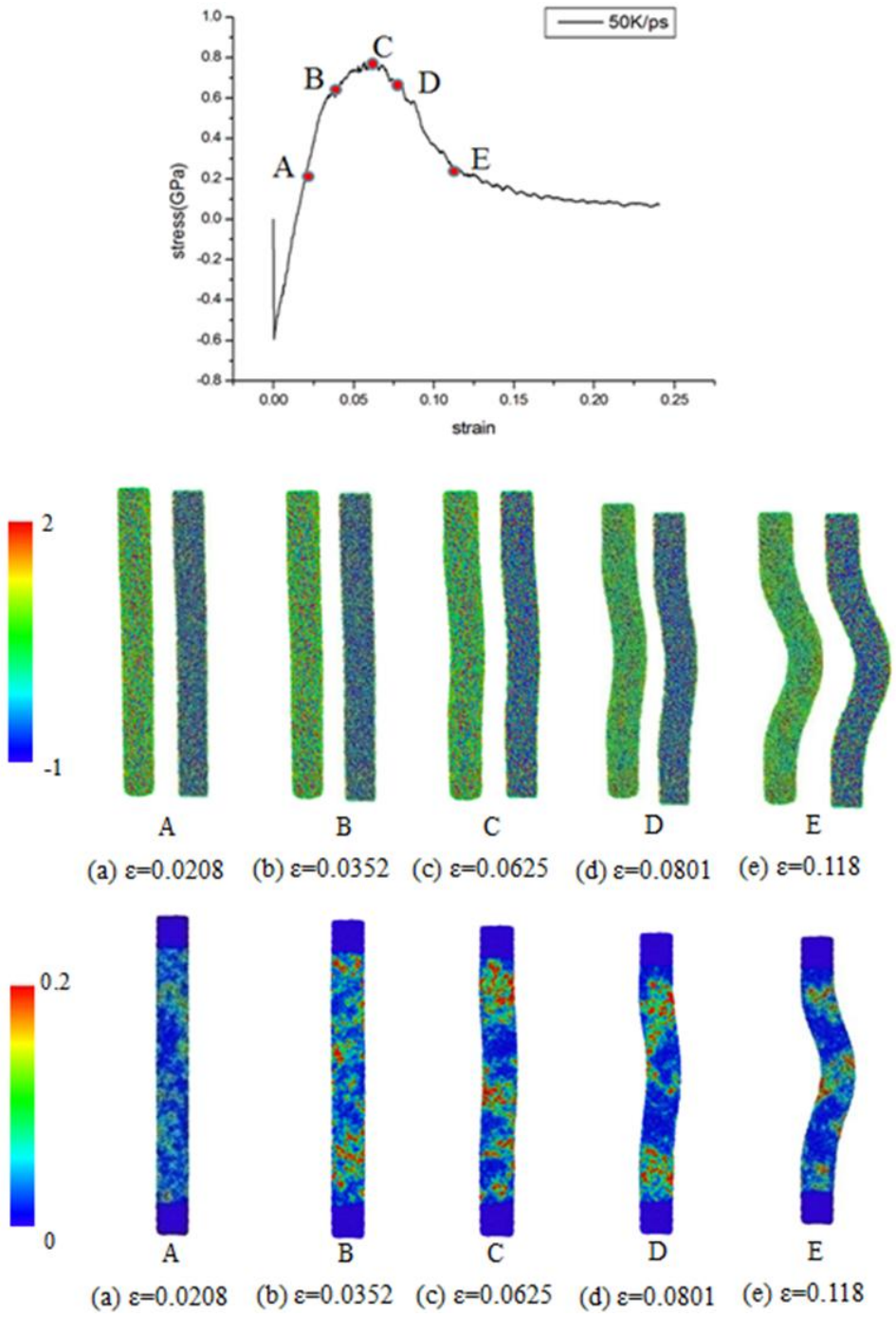

Figure 8. Stress–strain curves, deformation mechanism, and distributions of local stress viewed from surface and section (second row) and local shear strain (third row) of $Ni_{50}Al_{50}$ NWs at different strains with quenching rates of 50 K/ps (L/D = 10, T = 100 K).

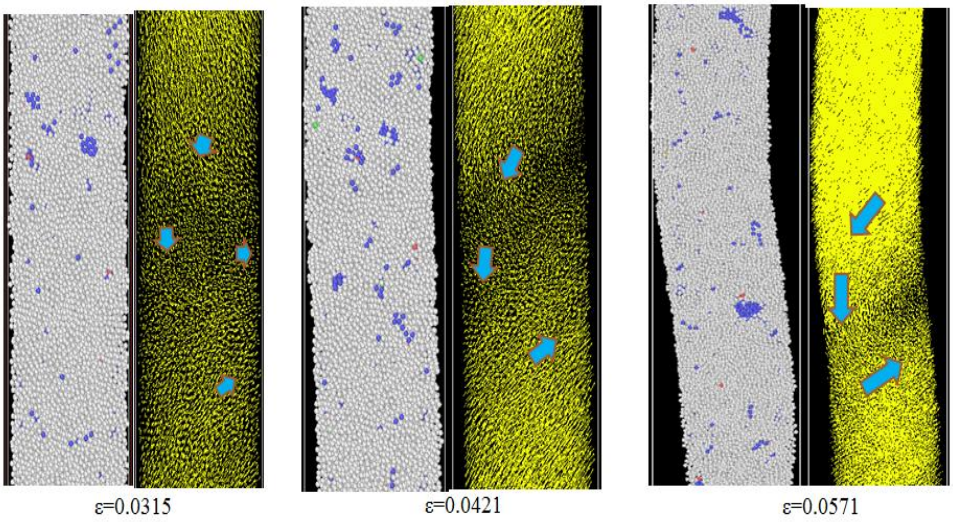

Figure 9. Atomic displacement vectors (RHS of each strain level) and distribution of microstructures (LHS: gray: amorphous; blue: BCC) of $Ni_{50}Al_{50}$ NWs at different compression stages with quenching rates of 50 K/ps (L/D = 15, T = 100 K).

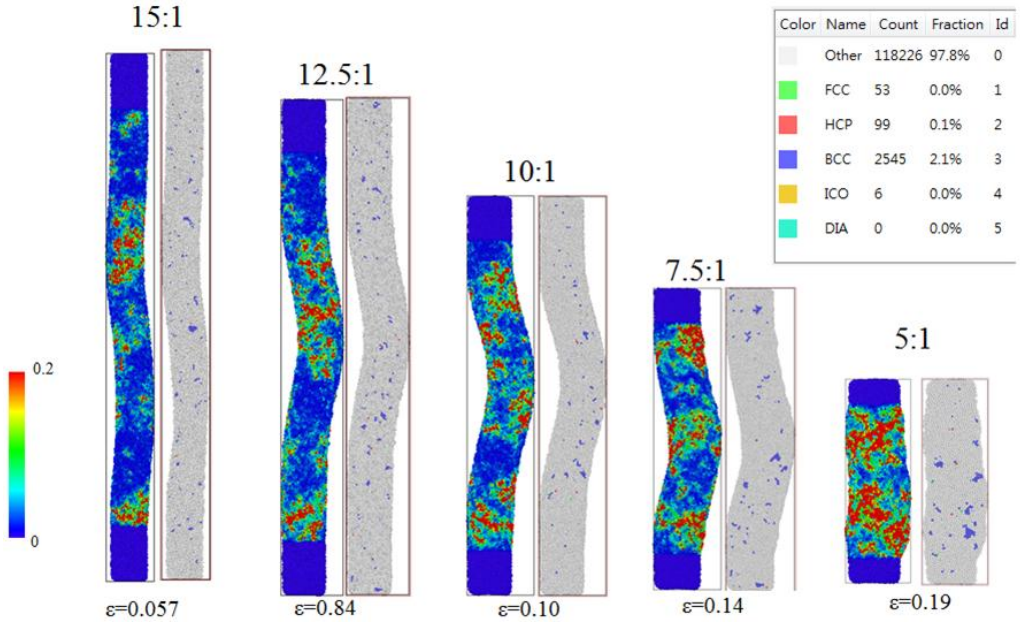

Figure 10. Deformation mechanism, local shear strain (LHS of each strain level), and distributions of microstructures (RHS: gray: amorphous; blue: BCC) of $Ni_{50}Al_{50}$ NWs at different slenderness ratios with quenching rates of 50 K/ps (T = 100 K).

The stress–strain curves of NWs at the quenching rate of 5 K/ps with the different alloy ratios and the slenderness ratios of 5 and 15 are as shown in Figures 11 and 12, respectively. It can be seen that the ultimate stress generally increases with the increase of the content of Al. However, B2 phase of $Ni_{50}Al_{50}$ always exhibits the highest ultimate stress. The ultimate stress of this alloy at the higher slenderness ratio is smaller than that at the lower slenderness ratio due to the different deformation mechanisms. Moreover, the discrepancy in ultimate stress is much more significant when the

slenderness ratio is lower. It means that much greater stress is required to induce the extrudes in NWs. Distributions of local shear strain and deformation pattern of NWs with quenching rates 5 K/ps at L/D = 5 with different alloy ratios at ultimate stress are depicted as in Figure 13. There exists no significant difference between NWs with different alloy ratios. Distributions of local shear strain and deformation pattern of NWs at slenderness ratio of 15 and quenching rates of 5 K/ps with different alloy ratios at ultimate stress are as shown in Figure 14. There still exists no significant difference in the distributions of local shear strain. However, NWs of $Ni_{50}Al_{50}$ and $Ni_{20}Al_{80}$ alloys are a little bit more susceptible to buckling than the other NiAl alloys.

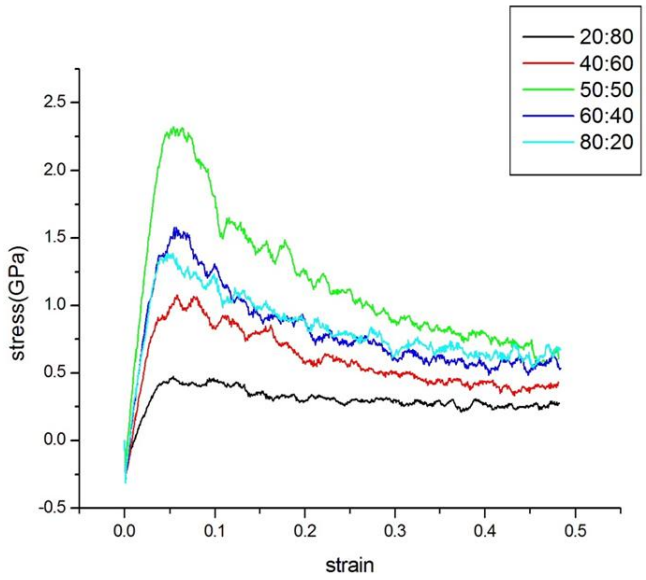

Figure 11. Stress–strain curves of NWs at L/D = 5 with different alloy ratios (quenching rate: 5 K/ps, T = 100 K).

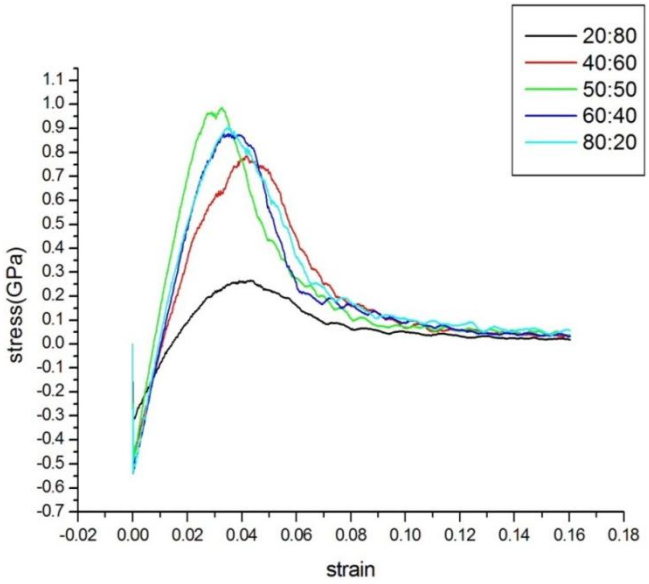

Figure 12. Stress–strain curves of NWs at L/D = 15 with different alloy ratios (quenching rates: 5 K/ps, T = 100 K).

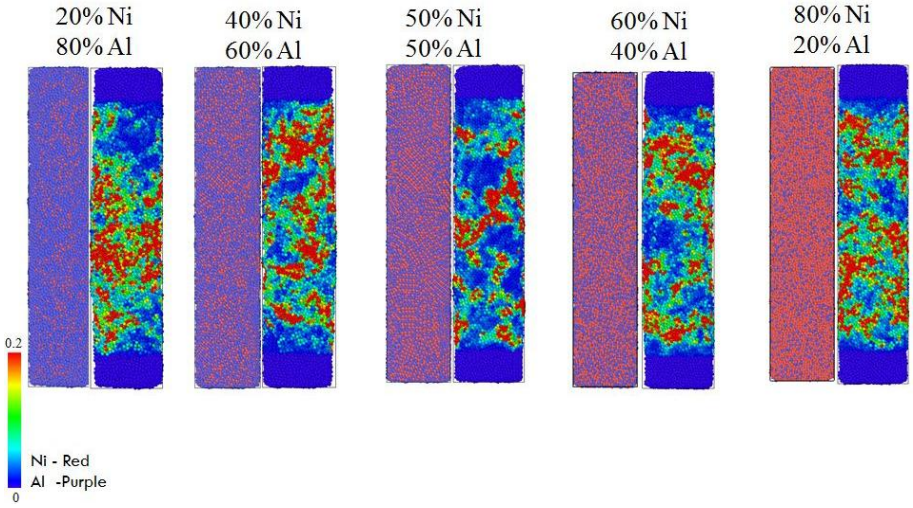

Figure 13. Distributions of local shear strain (RHS of each alloy ratio) and atoms (LHS: purple: Al; red: Ni) as well as deformation pattern of NWs at L/D = 5 with different alloy ratios at ultimate stress (quenching rates: 5 K/ps, T = 100 K).

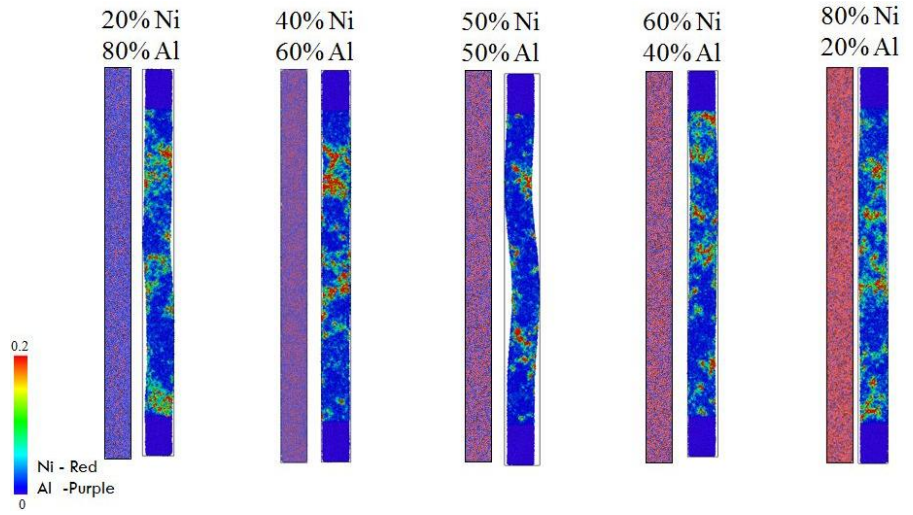

Figure 14. Distributions of local shear strain (RHS of each alloy ratio) and atoms (LHS: purple: Al; red: Ni) as well as deformation pattern of NWs at L/D = 15 with different alloy ratios at ultimate stress (quenching rates: 5 K/ps, T = 100 K).

As shown in Figures 15 and 16, the effects of temperature on ultimate stress are insignificant as the quenching rate is within the range of 5 to 50 K/ps. However, the ultimate stress decreases with the increase of temperature as the quenching rate is 0.5 K/ps. Moreover, as shown in Figures 17–19, when the strain rate increases from 0.05 to 0.5 %/ps, the ultimate stress is significantly enhanced especially for the structure with high slenderness ratio. Moreover, the phenomenon of buckling is more significant for lower strain rate, as shown in Figure 20. It is known that higher-energy buckling modes, instead of fundamental buckling mode, will be actuated by the faster compression rate, as reported in [33]. Therefore, it needs larger compressive force to induce buckling. In other words, the

phenomenon of buckling is more difficult taken place as the strain rate is higher. In comparison Figures 17 with 18, it can be found that the ultimate stresses of NWs with slenderness ratio of 15 and 5 are 1.9 GPa and 2.9 GPa, respectively. Since the NWs with large slenderness ratio and small strain rate tend to deform by buckling, they are deformed by buckling when the strain rate is ranged 0.05–0.2 %/ps and only a small amount of energy can be absorbed. On the other hand, when the strain rate is as high as 0.5 %/ps, a significant amount of energy can be sustained by the NWs when the slenderness ratio equals 15. On the other hand, the NWs are always deformed by compressive deformation without inducing buckling as the slenderness ratios is equal to 5.

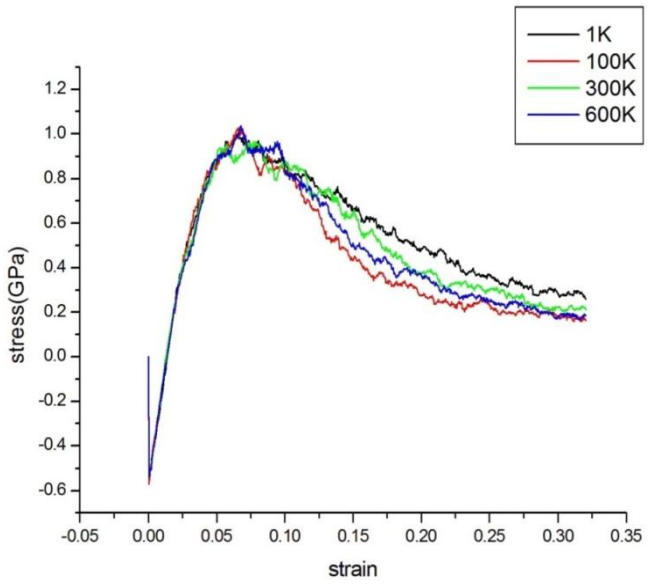

Figure 15. Stress–strain curves of $Ni_{50}Al_{50}$ NWs with quenching rates of 50 K/ps at different temperatures (L/D = 10).

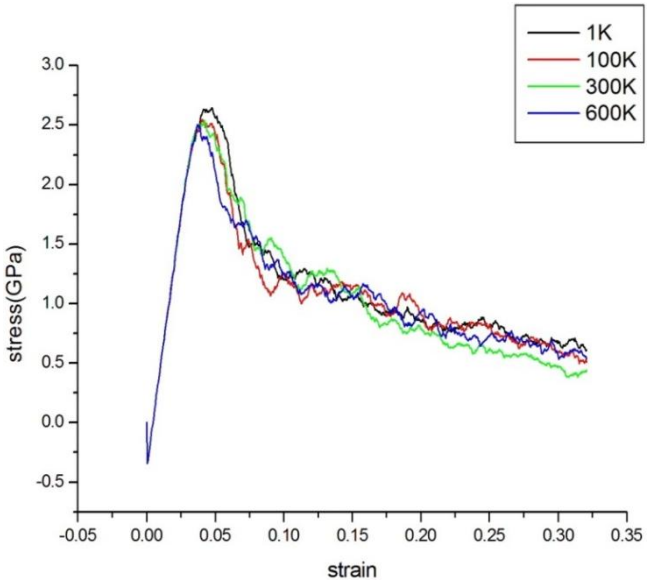

Figure 16. Stress–strain curves of $Ni_{50}Al_{50}$ NWs with quenching rates of 0.5 K/ps at different temperatures (L/D = 10).

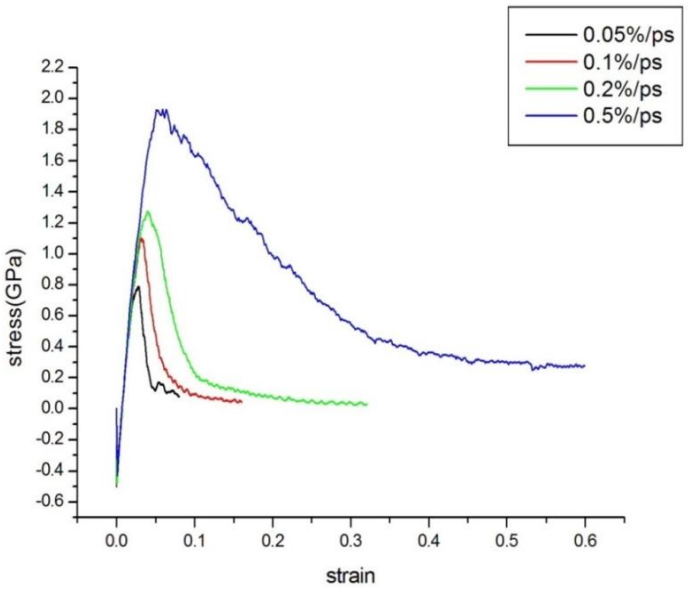

Figure 17. Stress–strain curves of $Ni_{50}Al_{50}$ NWs with quenching rates of 5 K/ps at different strain rates (L/D = 15, T = 100 K).

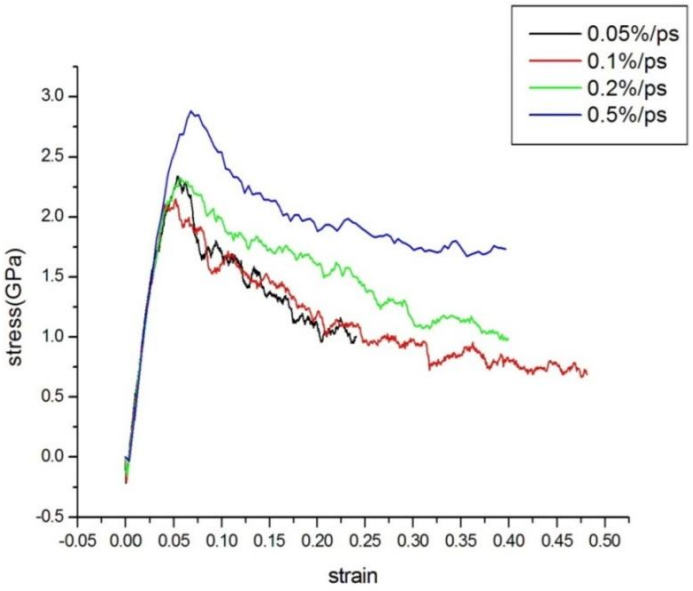

Figure 18. Stress–strain curves of $Ni_{50}Al_{50}$ NWs with quenching rates of 5 K/ps at different strain rates (L/D = 5, T = 100 K).

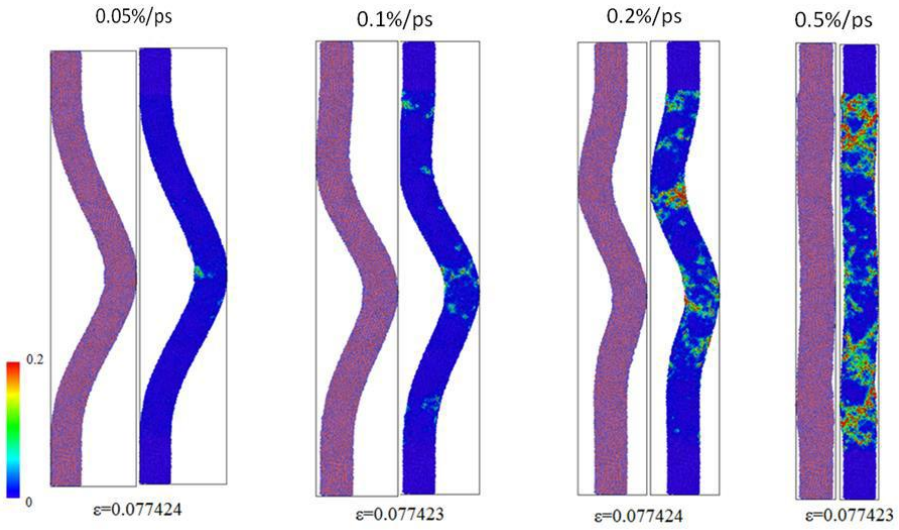

Figure 19. Deformation pattern as well as distributions of local shear strain (RHS of each strain level) and atoms (LHS: purple: Al; red: Ni) of $Ni_{50}Al_{50}$ NWs at L/D = 15 and different strain rates (quenching rates: 5 K/ps, T = 100 K).

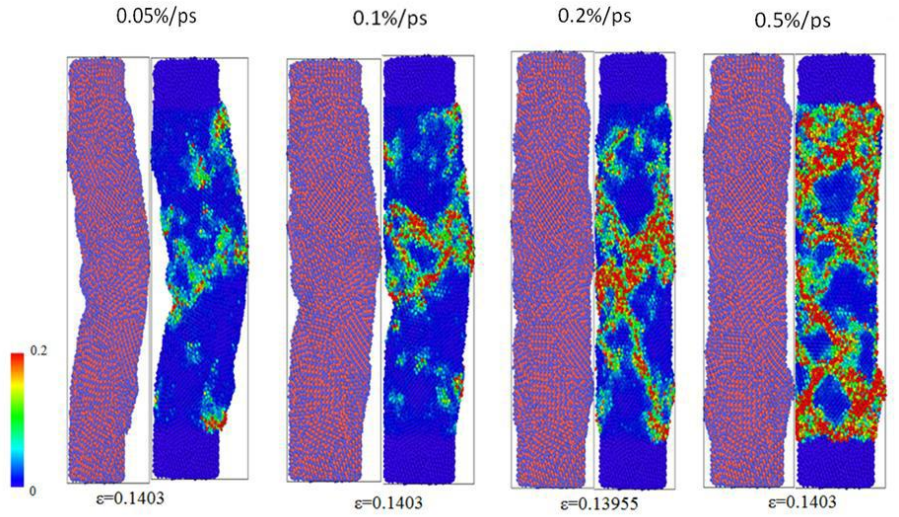

Figure 20. Deformation pattern as well as distributions of local shear strain (RHS of each strain level) and atoms (LHS: purple: Al; red: Ni) of $Ni_{50}Al_{50}$ NWs at L/D = 5 and different strain rates (quenching rates: 5 K/ps, T = 100 K).

The effects of percentage of point defects on the microstructures of $Ni_{50}Al_{50}$ NWs using CNA technique at quenching rate of 0.5 K/ps are as shown in Figure 21. It is observed that the point defects provide a good condition for the reformation of amorphous phase. The percentage of amorphous phase increases very fast from 43.6 to 81.1% as the point defect is increasing from 0 to 10%. Figures 22 and 23 indicate that the effects of point defect concentration on ultimate stress are insignificant for high quenching rate and become remarkable for low quenching rate. For instance, the ultimate decreases from 1.7 to 1.2 GPa as the point defect concentration increases from perfect 0

to 10% point defect concentration at low quenching rate of 0.5 K/ps. However, it almost remains unchanged at high quenching rate of 50 K/ps. In other words, the effect of point defect on ultimate stress is more significant for the materials with crystalline phase rather than with amorphous phase. For the structure with a large amount of amorphous phase and low slenderness ratio, shear bands are significantly induced. It is interesting to find that when the percentage of defects increases, not only the grain size is decreased but also the amount of amorphous phase is remarkably increased. In other words, the appearance of point defects tends to enhance the formation of amorphous phase and induce small nano-grained microstructure in the material.

For the $Ni_{50}Al_{50}$ NWs prepared by a high quenching rate of 50 K/ps, as depicted in Figure 22, the stress–strain curves are quite similar when the percentage of point defects is within the range from 0 to 10%. This result can be explained by the fact that since almost all the microstructures become amorphous phase under this high quenching rate, the concentration of point defects has nearly no influence on the change of microstructures. Consequently, one can find that quite similar stress–strain curves appear under the action of uniaxial compressive stress. On the contrary, when the NWs are fabricated with a low quenching rate of 0.5 K/ps, as shown in Figure 23, the effects of the percentage of point defects on the stress–strain curves become much more significant. Much lower ultimate stress can be found for the case with 10% point defects. Distributions of the local shear strain and the deformation pattern of $Ni_{50}Al_{50}$ NWs at a slenderness ratio of 10 and a quenching rate of 0.5 K/ps with different percentage of point defects are as shown in Figure 24. It is found that the deformation mechanisms change from extrude-like to the combination of the compressive deformation and the buckling as the percentage of point defects increases from 0 to 10%.

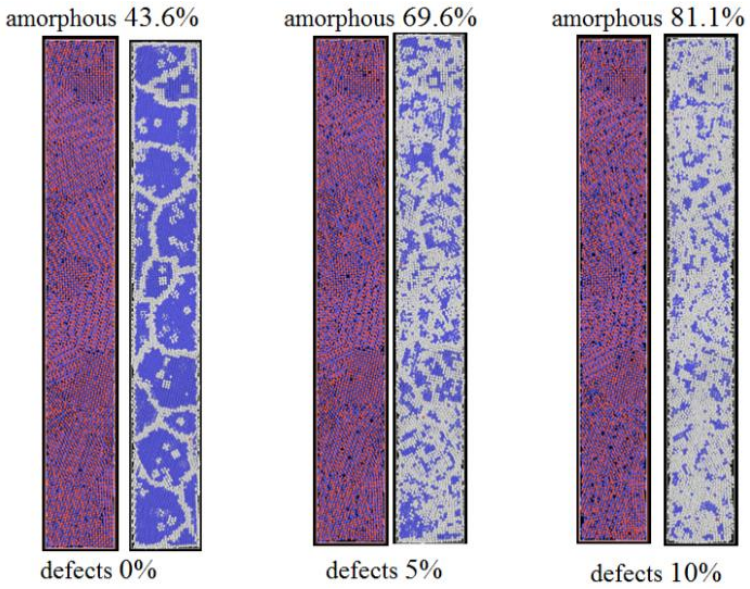

Figure 21. Distributions of atoms (LHS of each percentages of defects: purple: Al; red: Ni) and microstructures (RHS: gray: amorphous; blue: BCC) at quenching rate of 0.5 K/ps with different percentage of point defects ($Ni_{50}Al_{50}$, L/D = 10, T = 100 K).

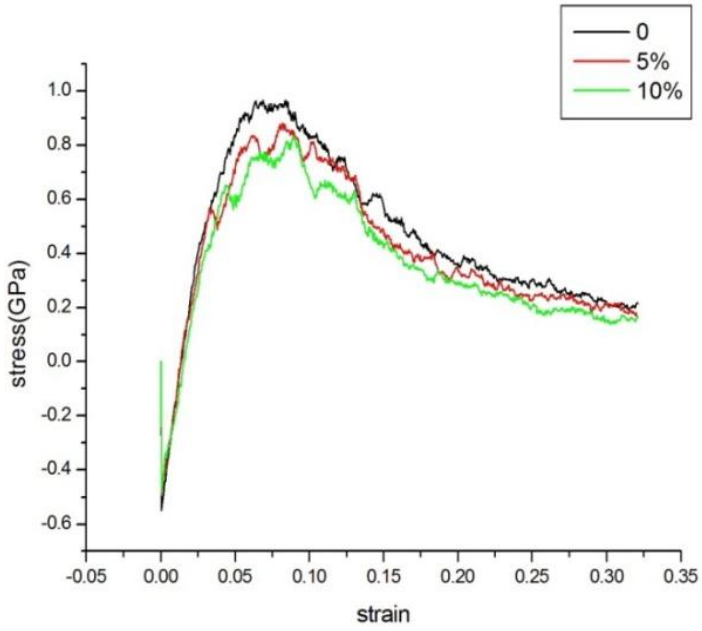

Figure 22. Stress–strain curves of $Ni_{50}Al_{50}$ NWs at quenching rate of 50 K/ps with different percentage of point defects (L/D = 10, T = 100 K).

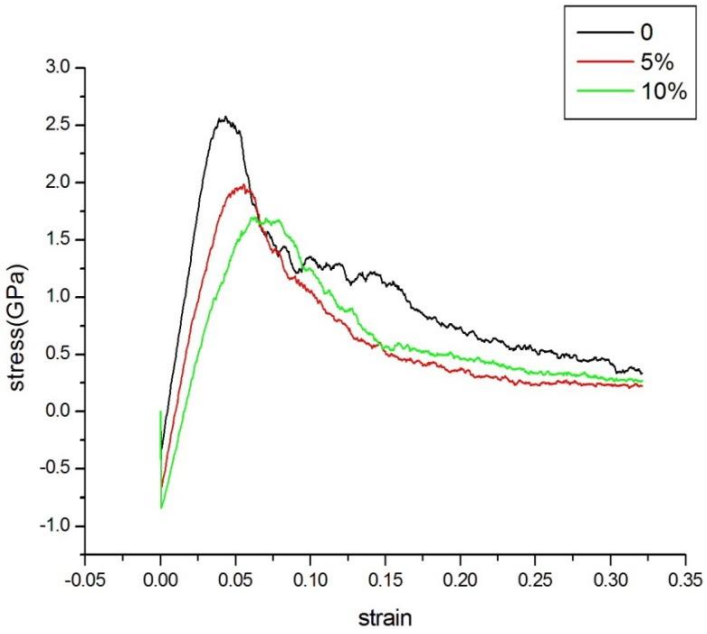

Figure 23. Stress–strain curves of $Ni_{50}Al_{50}$ NWs at quenching rate of 0.5 K/ps with different percentage of point defects (L/D = 10, T = 100 K).

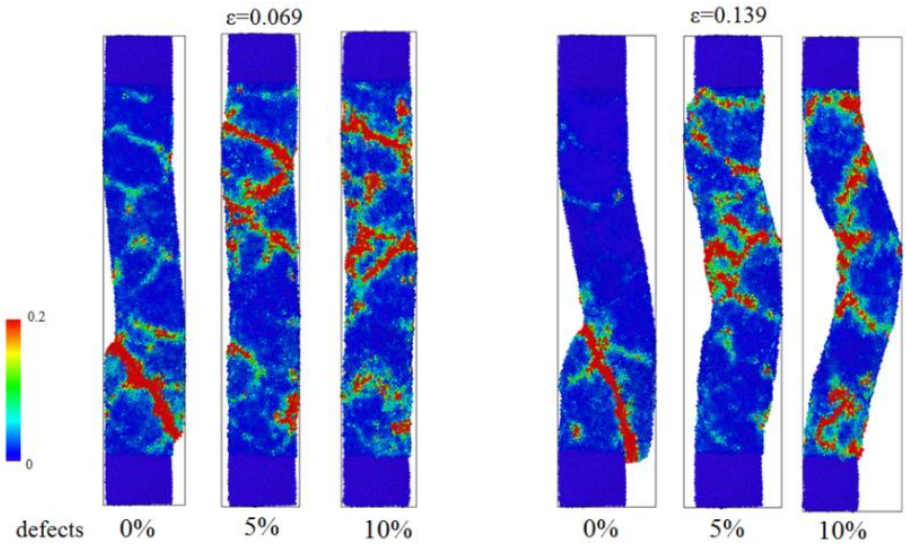

Figure 24. Distributions of local shear strain and deformation pattern of $Ni_{50}Al_{50}$ NWs at quenching rate of 0.5 K/ps with different percentage of point defects ($Ni_{50}Al_{50}$, L/D = 10, T = 100 K).

4. Conclusion

Simulation results are summarized that under the same conditions of alloy ratio, strain rate and temperature, the ultimate stress and Young's modulus of NWs are increased with the decrease of quenching rate. Moreover, the ultimate stress becomes higher as the slenderness ratio is smaller. As the slenderness ratio is higher than 10, the calculated ultimate stresses are in good agreement with modified Euler's formula. When the quenching rate and slenderness ratio are low, the NWs are significantly deformed along the slip system. However, the phenomena of the buckling take place as the slenderness ratio and quenching rate are increased. On the other hand, shear bands appear significantly for the cases with small slenderness ratio at high quenching rate. For different alloy ratios, the ultimate stress and Young's modulus, in general, are increasing with the increase of Ni content. However, B2 phase $Ni_{50}Al_{50}$ exhibits the highest ultimate stress and Young's modulus. The effect of temperature on ultimate stress is insignificant as the quenching rate is within the range from 5 to 50 K/ps. However, the ultimate stress decreases with the increase of temperature as the quenching is 0.5 K/ps.

Acknowledgments

The authors gratefully acknowledge the financial support provided to this study by the Ministry of Science and Technology (MOST) of Taiwan under contract No. 106-2221-E-006-103.

Conflict of interest

All authors declare no conflicts of interest in this paper.

References

1. Swain M, Singh S, Basu S, et al. (2014) Identification of a kinetic length scale which dictates alloy phase composition in Ni-Al interfaces on annealing at low temperatures. *J Appl Phys* 116: 222208.
2. Liu E, Jia J, Bai Y, et al. (2014) Study on preparation and mechanical property of nanocrystalline NiAl intermetallic. *Mater Design* 53: 596–601.
3. Vitali E, Wei CT, Benson DJ, et al. (2011) Effects of geometry and intermetallic bonding on the mechanical response, spalling and fragmentation of Ni–Al laminates. *Acta Mater* 59: 5869–5880.
4. Zhang W, Peng Y, Liu Z (2014) Molecular dynamics simulations of the melting curve of NiAl alloy under pressure. *AIP Adv* 4: 057110.
5. Darolia R (1994) Structural applications of NiAl. *J Mater Sci Technol* 10: 157–167.
6. Bei H, George EP (2005) Microstructures and mechanical properties of a directionally solidified NiAl–Mo eutectic alloy. *Acta Mater* 53: 69–77.
7. Lee JY, Han KH, Park JM, et al. (2006) Deformation and evolution of shear bands under compressive loading in bulk metallic glasses. *Acta Mater* 54: 5271–5279.
8. Alavi A, Mirabbaszadeh K, Nayebi P, et al. (2010) Molecular dynamics simulation of mechanical properties of Ni–Al nanowires. *Comp Mater Sci* 50: 10–14.
9. Wang Q, Yang Y, Jiang H, et al. (2014) Superior tensile ductility in bulk metallic glass with gradient amorphous structure. *Sci Rep* 4: 4757–4762.
10. Jang D, Greer JR (2010) Transition from a strong-yet-brittle to a stronger-and-ductile state by size reduction of metallic glasses. *Nat Mater* 9: 215–219.
11. Guo SF, Qiu JL, Yu P, et al. (2014) Fe-based bulk metallic glasses: brittle or ductile? *Appl Phys Lett* 105: 161901.
12. Jiang MQ, Wilde G, Jiang F, et al. (2015) Understanding ductile-to-brittle transition of metallic glasses from shear transformation zone dilatation. *Theor Appl Mech Lett* 5: 200–204.
13. Xi XK, Zhao DQ, Pan MX, et al. (2005) Fracture of brittle metallic glasses: Brittleness or plasticity. *Phys Rev Lett* 94: 125510.
14. Sopu D, Foroughi A, Stoica M, et al. (2016) Brittle-to-ductile transition in metallic glass nanowires. *Nano Lett* 16: 4467–4471.
15. Wu FF, Zhang ZF, Mao SX, et al. (2009) Effect of sample size on ductility of metallic glass. *Phil Mag Lett* 89: 178–184.
16. Tian L, Wang XL, Shan ZW (2016) Mechanical behavior of micronanoscaled metallic glasses. *Mater Res Lett* 4: 63–74.
17. Magagnosc DJ, Ehrbar R, Kumar G, et al. (2013) Tunable tensile ductility in metallic glasses. *Sci Rep* 3: 1096.
18. Chen DZ, Jang D, Guan KM, et al. (2013) Nanometallic glasses: size reduction brings ductility, surface state drives its extent. *Nano Lett* 13: 4462–4468.
19. Wang Z, Mook WM, Niederberger C, et al. (2012) Compression of nanowires using a flat indenter: diametrical elasticity measurement. *Nano Lett* 12: 2289–2293.
20. Hwang B, Kim T, Han SM (2016) Compression and tension bending fatigue behavior of Ag nanowire network. *Extreme Mech Lett* 8: 266–272.

21. Wang J, Hodgson PD, Zhang J, et al. (2010) Effects of pores on shear bands in metallic glasses: A molecular dynamics study. *Comp Mater Sci* 50: 211–217.
22. Wang JG, Chan KC, Fan JC, et al. (2014) Buckling of metallic glass bars. *J Non-Cryst Solids* 387: 1–5.
23. Wachter J, Gutiérrez G, Zúniga A, et al. (2014) Buckling of Cu–Zr-based metallic glasses nanowires: molecular dynamics study of surface effects. *J Mater Sci* 49: 8051–8056.
24. Sung PH, Chen TC (2016) Effects of quenching rate on crack propagation in NiAl alloy using molecular dynamics. *Comp Mater Sci* 114: 13–17.
25. Zhuo XR, Beom HG (2019) Effect of side surface orientation on the mechanical properties of silicon nanowires: a molecular dynamics study. *Crystals* 9: 102.
26. Cao LX, Shang JX, Zhang Y (2009) Molecular dynamics simulation of stress-induced martensitic phase transformation in NiAl. *Acta Phys Sin-Ch Ed* 58: 7307–7312.
27. Pun GPP, Mishin Y (2010) Molecular dynamics simulation of the martensitic phase transformation in NiAl alloys. *J Phys-Condens Mat* 22: 395403.
28. Mortazavi B, Cuniberti G, Rabczuk T (2015) Mechanical properties and thermal conductivity of graphitic carbon nitride: A molecular dynamics study. *Comp Mater Sci* 99: 285–289.
29. Murray JL (1986) Binary alloy phase diagrams. ASM International, Materials Park, OH.
30. Daw MS, Baskes MI (1984) Embedded-atom method: Derivation and application to impurities, surfaces, and other defects in metals. *Phys Rev B* 29: 6443–6452.
31. Kelchner CL, Plimpton SJ, Hamilton JC (1998) Dislocation nucleation and defect structure during surface indentation. *Phys Rev B* 58: 11085–11088.
32. Wang GF, Feng XQ (2009) Surface effects on buckling of nanowires under uniaxial compression. *Appl Phys Lett* 94: 141913.
33. Jiang JW (2015) The strain rate effect on the buckling of single-layer MoS_2. *Sci Rep* 5: 7814.

AIMS Press